HHS Public Access

Author manuscript

Brain Struct Funct. Author manuscript; available in PMC 2019 December 01.

Published in final edited form as:

Brain Struct Funct. 2018 December ; 223(9): 3945–3958. doi:10.1007/s00429-018-1731-0.

Claustrum circuit components for top-down input processing and cortical broadcast

Michael G. White and **Brian N. Mathur***

Department of Pharmacology, University of Maryland, School of Medicine, Baltimore, MD, USA 21201

Abstract

Anterior cingulate cortex (ACC) input to the claustrum is required for top-down cognitive control of action. By virtue of its widespread cortical connectivity, the claustrum is anatomically situated to process and broadcast top-down signals from ACC to downstream cortices. In order to gain a deeper understanding of claustrum processing mechanisms, it is first critical to identify the projection neuron subtypes within claustrum, the intrinsic and extrinsic components regulating their firing, and the differential innervation of cortex by projection neuron subtypes. To this end, we used whole-cell patch clamp electrophysiology in adult mouse brain slices to distinguish two spiny projection neuron subtypes in claustrum, referred to as type I and II neurons, and three aspiny interneuron subtypes, referred to as type III, IV, and V neurons. In response to optogenetic ACC afferent stimulation, type II neurons preferentially burst fire relative to type I neurons. This burst firing is calcium-dependent and is optimized by voltage-gated potassium channels. Lastly, we find that visual cortices, parietal association cortex, and ACC receive input from type I and II neurons in differing proportions. These data reveal the diversity of claustrum neurons and mechanisms by which claustrum processes ACC command for spatiotemporal coordination of the cerebral cortex.

Keywords

anterior cingulate cortex; visual cortices; parietal association cortex; burst fire; membrane properties

Introduction

The anterior cingulate cortex (ACC) provides a dense input to the claustrum (Smith and Alloway 2010; Atlan et al. 2017; Wang et al. 2017; White et al. 2017, 2018) that encodes a top-down preparatory signal necessary for optimal cognitive control of action (White et al.

*Correspondence to: Brian N. Mathur, BRB 4-011, 655 West Baltimore Street, Baltimore, MD 21201, Tel: (410) 706-8239, bmathur@som.umaryland.edu.

Author contributions: M.G.W. and B.N.M. designed research, generated and analyzed data, and wrote the manuscript.

Conflicts of interest: The authors declare no conflicts of interest.

Compliance with Ethical Standards: The authors declare no financial and non-financial competing interests. All applicable international, national, and/or institutional guidelines for the care and use of animals were followed. All procedures performed in studies involving animals were in accordance with the ethical standards of the institution or practice at which the studies were conducted.

2018). Claustrum projection neurons target many cortical areas (Crick and Koch 2005; Mathur 2014; White et al. 2017), functionally link ACC to visual and parietal cortices (White and Mathur 2018) and burst fire in response to incoming ACC signals (White et al. 2018; White and Mathur 2018). Claustrum inhibitory microcircuitry constrains this burst firing response to sculpt claustrum transformation of ACC signals (White et al. 2018). Identifying the claustrum projection neuron and inhibitory interneuron subtypes is critical to understand how this enigmatic, yet highly cortically interconnected nucleus processes top-down signals that may influence large swaths of cerebral cortex.

Extant anatomical evidence distinguishes spiny glutamatergic projection neurons from aspiny GABAergic interneurons (Braak and Braak 1982; Hur and Zaborszky 2005; Watakabe et al. 2014). Calcium binding protein expression further delineates subtypes of aspiny interneurons, including parvalbumin (PV)- expressing neurons in rodents (Real et al. 2003; Dávila et al. 2005) and other species (Reynhout and Baizer 1999; Wójcik et al. 2004; Rahman and Baizer 2007; Kowiański et al. 2009; Cozzi et al. 2014; Szalak et al. 2015; Pirone et al. 2015), including human (Pirone et al. 2014; Hinova-Palova et al. 2014). PV-positive and PV-negative interneurons provide feedforward inhibition onto spiny projection neurons (Kim et al. 2016; White et al. 2018). Specific interrogation of microcircuit responsivity to ACC afferent stimulation demonstrates monosynaptic excitatory drive onto both spiny projection neurons and interneuron subtypes (White et al. 2018). In the absence of $GABA_A$-mediated synaptic transmission, claustrum projection neurons exhibit epileptiform-like activity in response to ACC drive (White et al. 2018), underscoring the influence of inhibitory microcircuitry for shaping claustrum output.

Ultimately, claustrum projection neurons receiving ACC input provide output to downstream cortical sites (White et al. 2018). However, it is unclear if burst firing is a processing feature of all claustrum spiny neurons or if claustrum projection neuron subtypes differentially innervate cortex. To more clearly elucidate how claustrum processes incoming ACC information for broadcast to downstream cortical sites, we applied standard electrophysiological measures that are widely available in neuroscience labs. We discover that passive and active membrane properties reveal the presence of two subtypes of spiny projection neurons (types I and II) and three subtypes of aspiny interneurons (types III-V) in the adult mouse claustrum. We find that burst firing in response to ACC stimulation is an intrinsic membrane property and predominantly occurs in type II neurons. Further, we find that type I neurons preferentially innervate visual cortices, whereas type II neurons preferentially innervate the ACC. These findings inform interrogations into pathological changes in claustrum, which may ultimately contribute to disease states involving dysregulation of cortical function (Morys et al. 1996; Kong et al. 2012; Patru and Reser 2015; Bernstein et al. 2016).

Materials and Methods

Animals.

68 C57BL/6J wildtype mice, transgenic mice encoding *cre* recombinase in the PV gene (*PV-cre*; Tanahira et al. 2009; Mathur et al. 2013), and transgenic mice encoding *TdTomato* flanked by *loxP* sites (Madisen et al. 2010) crossed with *PV-cre* mice (*PV-cre* × *FloxTdTom*)

of both sexes were used for this study. Mice were 10-34 weeks of age at the time of experiments, group-housed with food and water available *ad libitum*, and on a 12 hr light/dark cycle that begin at 0700 each day. This study was performed in accordance with the National Institutes of Health Guide for Care and Use of Laboratory Animals and the University of Maryland, School of Medicine, Animal Care and Use Committee.

Viral vectors, retrograde tract tracing and stereotaxic procedures.

Mice were anesthetized via inhalation of 3% isoflurane before being placed in a stereotaxic frame and anesthesia was maintained with inhalation of 1% isoflurane. A small craniotomy over the brain area of interest was made prior to viral or retrograde tract tracer injection. For the viral injections into ACC, 150-185 nL of an adeno-associated virus (AAV) vector expressing channelrhodopsin-2 (H134R mutation) and an mCherry fluorescent tag under the *CAG* promoter (AAV5-CAG-ChR2-mCherry; University of Pennsylvania Vector Core) was injected bilaterally at two rostrocaudal levels of the ACC (4 total injections). Post-surgery survival time was a minimum of 4 weeks to permit adequate viral expression. For retrograde tract tracing, we injected bilaterally 125 nL of the retrogradely transported form of BDA conjugated with Texas Red® (3,000 MW; Thermo Fisher Scientific) into either primary/secondary visual cortex (V1/V2), parietal association cortex (PtA), or ACC at a single rostrocaudal level. Post-surgery survival time was approximately one week to allow adequate retrograde transport.

Relative to bregma (dorsal-ventral coordinates were measured from the brain surface), the coordinates for viral injections into ACC were 1) anterior (A)-posterior (P): +1.34 mm, medial (M)-lateral (L): ± 0.30 mm, dorsal (D)-ventral (V): −1.25 mm; and 2) A-P: +0.74 mm, M-L: ± 0.30 mm, D-V: −1.00 mm. The coordinates A-P: +1.00 mm, M-L: ± 0.30 mm, D-V: −1.20 mm were used for retrograde tracer injections into ACC. The coordinates for V1/V2 retrograde tracer injections were A-P: −2.90 mm, M-L: ± 2.05 mm, D-V: −0.40 mm, and coordinates for PtA retrograde tracer injections were A-P: −1.90 mm, M-L ± 1.40 mm, D-V: −0.40 mm.

Ex vivo brain slice preparation for electrophysiology.

Following anesthetization, mice were decapitated, the brains were extracted, and 250 μm coronal sections were sliced using a vibrating microtome in a high-sucrose artificial cerebrospinal fluid (aCSF). The aCSF was ice-cold, carbogen (95% O_2, 5% CO_2)-bubbled, and consisted of 194 mM sucrose, 30 mM NaCl, 4.5 mM KCl, 1 mM $MgCl_2$, 26 mM $NaHCO_3$, 1.2 mM NaH_2PO_4, and 10 mM D-glucose. Sections were incubated after slicing for 30 min at 33°C in carbogen-bubbled aCSF (315-320 mOsm) that contained 124 mM NaCl, 4.5 mM KCl, 2 mM $CaCl_2$, 1 mM $MgCl_2$, 26 mM $NaHCO_3$, 1.2 mM NaH_2PO_4, and 10 mM D-glucose. Sections were incubated at room temperature until use for whole-cell patch-clamp recordings, and recordings were performed in the same aCSF formulation used for incubation.

Whole-cell current and voltage-clamp recordings.

Whole-cell recordings were performed at 29 -31°C using borosilicate glass recording pipettes of 3-7 MΩ resistance. For recordings performed in a current clamp configuration,

recording pipettes were filled with a potassium-based solution (290-295 mOsm; pH 7.3) composed of 126 mM potassium gluconate, 4 mM KCl, 10 mM HEPES, 4 mM ATP-Mg, 0.3 mM GTP-Na and 10 mM phosphocreatine. For recordings performed in a voltage-clamp configuration, recording pipettes were filled with a $CsMeSO_4$-based internal solution (300-310 mOsm; pH 7.3) composed of 114 mM $CsMeSO_4$, 5 mM NaCl, 1mM TEA-Cl, 10 mM HEPES, 5 mM QX-314, 1.1 mM EGTA, 0.3 mM Na-GTP, and 4 mM Mg-ATP. Clampex software (version 10.4; Molecular Devices; Sunnyvale, CA) was used for electrophysiological recordings, which were filtered at 2 kHz and digitized at 10 kHz. Internal pipette solutions also contained hydrazide dye conjugated with AlexaFluor®-488 (40 μM) and/or 3-5% neurobiotin for either real-time or post-hoc, respectively, localization of recorded neurons and visualization of dendritic spines. Retrogradely-labeled neurons projecting to V1/V2, PtA, or ACC were identified using epifluorescence and targeted for recordings. Each neuron was given a series of current injections in 100 pA intervals. Maximum firing rate of neurons was defined as the spike frequency during the largest current injection that did not result in depolarization block over the course of the current injection (500 ms). Voltage-gated cation current (VGCC) was elicited by performing a 50 mV voltage step (−60 to −10 mV) for 500 ms using the $CsMeSO_4$-based internal pipette solution.

Histochemistry and immunohistochemistry.

A specialized protocol to minimize lipid and aldehyde auto-fluorescence was utilized (Kupferschmidt et al. 2015) for histochemistry and immunohistochemistry of 250 μm brain slices used for whole-cell electrophysiology. This protocol was used to illustrate expression of ACC terminals in claustrum and claustrum neurons targeted for whole-cell recordings. For these slices, primary rabbit anti-mCherry antibody (1:500; Abcam, Cambridge, MA) and secondary donkey anti-rabbit antibody conjugated to Cy3 (1:500; Jackson ImmunoResearch, West Grove, PA) were used to label viral expression of mCherry protein. Streptavidin conjugated to AlexaFluor®-488 (1:1,000; Jackson ImmunoResearch) was used to label neurobiotin-filled neurons.

To obtain representative images of retrograde tract tracer injections, mice injected with retrograde BDA were transcardially perfused with room temperature 0.1M phosphate-buffered saline (PBS), pH 7.2-7.4, followed by ice-cold 4% (weight/volume) paraformaldehyde in PBS. After the brain was extracted, brains were post-fixed with 4% paraformaldehyde in PBS overnight at 4°C. Coronal sections were sliced using an Integraslice 7550 MM vibrating microtome (Campden Instruments, Loughborough, England) at a thickness of 50 μm. Sections were immediately mounted and imaged to visualize retrograde BDA fluorescence.

Data analysis and statistics.

Electrophysiology data were analyzed using Clampex software (version 10.4). Statistical analyses were performed in GraphPad (Prism) or R statistical packages (version 3.2.3). To assess if the distribution of membrane properties was unimodal or bimodal, the fit of a single Gaussian or sum of two Gaussian curves to the distribution was compared. To assess spike

accommodation of neurons during current injection, accommodation index (AI) was calculated as defined previously (Druckmann et al. 2007):

$$AI = \frac{1}{N-k-1}\sum_{i=k}^{N}\frac{isi_i - isi_{i-1}}{isi_i + isi_{i-1}}$$

In this equation N is the number of action potentials, k is the number of initial action potentials to exclude, and ISI is the inter-spike interval. The convention k = 4 was used initially. This AI calculation returns the average normalized change in inter-spike interval across all spikes, and AI was calculated across the 500 ms current injection used to calculate the maximum firing rate. AI was also calculated for spiny projection neurons for the first 6 APs with k = 0 at the current injection below the current injection eliciting maximal firing. For analyses of basic membrane properties, a normal distribution was assumed and one-way ANOVAs were performed with neuron type as the factor of interest. For one-way ANOVAs reaching statistical significance, post-hoc Tukey's tests were performed in which the mean membrane property of interest for each cell type was compared to all other cell types.

Results

Membrane properties delineate two claustrum spiny projection neurons

A major concern for any study of the rodent claustrum is accurate identification of the structure relative to neighboring insular cortex and striatum. Previous studies suggest that dense connectivity of claustrum with ACC is isomorphic with claustrum-specific markers in the rodent (Mathur et al. 2009; White et al. 2017, 2018). Therefore, we injected the ACC of adult mice with a viral vector that expresses channelrhodopsin-2 and mCherry (AAV-ChR2-mCherry; Figure 1A). The dense, specific ACC innervation of claustrum identified the structure for whole-cell recordings (Figure 1B-1C) and allowed for contemporaneous stimulation of ACC afferents (White et al. 2017, 2018) in subsequent experiments. We differentiated claustrum spiny projection neurons from aspiny interneurons using recording pipettes filled with AlexaFluor®-488 to visualize dendritic spines (Figure 1D-1E).

To first identify potential subtypes of spiny projection neurons, we examined the distributions of passive membrane properties of these neurons ($n = 97$) to determine if any of the distributions were multimodal using a potassium-based internal pipette solution. We observed that the capacitance of spiny claustrum neurons exhibited a bimodal distribution (Figure 2A; single Gaussian fit $R^2 = 0.8038$, two Gaussian fit $R^2 = 0.9578$, F[3, 12] = 14.60, $P = 0.0003$), indicating the presence of two sub-types of claustrum spiny projection neurons: type I neurons ($n = 54$) characterized by smaller capacitance (118 ± 16 pF [mean ± SD]) and type II neurons ($n = 43$) characterized by significantly larger capacitance (158 ± 9.0 pF [mean ± SD]; Figure 2A). In contrast to capacitance, we observed unimodal distributions for resting membrane voltage (Figure 2B; single Gaussian $R^2 = 0.9193$, two Gaussian fit not estimable) and membrane resistance (Figure 2C; single Gaussian $R^2 = 0.8580$, two Gaussians $R^2 = 0.9084$, F[3, 8] = 1.468, $P = 0.2945$).

We next assessed the distributions of active membrane properties of claustrum spiny projection neurons ($n = 92$). Action potential (AP) threshold, which was measured during a current injection ramp (Figure 2D), exhibited a unimodal distribution (single Gaussian $R^2 = 0.8694$, two Gaussian fit not estimable; Figure 2E). Maximum firing rate also exhibited a unimodal distribution (single Gaussian $R^2 = 0.7625$, two Gaussians $R^2 = 0.8847$, F[3, 8] = 2.826, $P = 0.1067$; Figure 2F).

To examine differences in the intrinsic firing properties between type I ($n = 36$) and II ($n = 29$) neurons, we delivered depolarizing voltage steps. For both types, we observed action potential (AP) accommodation during the voltage step (Figure 2G). However, at the onset of depolarization, type II neurons exhibited a rapid AP burst and subsequent APs exhibited accommodation. The rapid AP burst was less evident in type I neurons and accommodation was not as apparent (Figure 2G). We calculated the accommodation index for the first 6 spikes and found that the index was indeed larger for type II neurons relative to type I neurons (unpaired *t* test, t[63] = 4.225, $P < 0.0001$; Figure 2H) and correlated with capacitance ($R^2 = 0.2949$, $P < 0.0001$; Figure 2H).

Membrane properties delineate three types of aspiny claustrum interneurons

Because the claustrum is richly PV-immunopositive (Mathur et al. 2009) and because PV+ interneurons typically exert powerful inhibitory control over projection neurons, we sought to differentiate PV− and PV+ interneurons. To this end, we used a *PV-cre* recombinase (*PV-cre*) mouse line (Tanahira et al. 2009; Mathur et al. 2013) crossed with mice expressing the TdTomato gene flanked by *loxP* sites (*FloxTdTom*; Madisen et al. 2010) to create *PV-cre/FloxTdTom* mice. In these mice we detected enriched TdTomato expression in claustrum corresponding to a minority population of aspiny interneurons that was consistent with prior immunohistochemical detection of PV in claustrum (Mathur et al. 2009; White et al. 2017, 2018). As such, the combined use of *PV-cre/FloxTdTom* mice and dye-filled recording pipettes allowed us to distinguish PV− and PV+ interneurons given that aspiny claustrum neurons are known interneurons (Brand 1981; Braak and Braak 1982). We used the convention of initially denoting PV− aspiny interneurons as type III claustrum neurons ($n = 43$) and denoting PV+ interneurons ($n = 25$) as at least a possible fourth subtype.

In response to a series of current injection steps, PV− interneurons ($n = 17$) consistently exhibited spike accommodation to positive current steps (Figure 3A). However, we observed two distinct firing phenotypes of PV+ interneurons in response to a depolarizing voltage step. Thus, we defined these neurons as type IV neurons ($n = 10$) characterized by fast-spiking (maximum firing rate > 150 Hz) with minimal spike accommodation (Figure 3B) and type V neurons ($n = 8$) characterized by slow-spiking (maximum firing rate < 100 Hz; Figure 3C) with spike accommodation (Figure 3C). We also observed that a majority of type V neurons were tonically active ($n = 8$ of 12; Figure 3D).

Examination of the distributions for spike accommodation and maximum firing rate for interneurons (Figure 3E-3F) segregated the PV+ type IV and V neurons. PV+ fast-spiking type IV neurons exhibited accommodation index and maximum firing rate values outside the range of values for all other aspiny neurons (significantly lower and higher, respectively). We also observed that PV+ interneurons had a bimodal distribution of resting membrane

voltage (single Gaussian R^2 = 0.5080, two Gaussians R^2 = 0.9151, F[3, 6] = 9.584, P = 0.0105), which segregated type IV neurons with a lower resting membrane voltage from type V neurons with a higher resting membrane voltage (Figure 3G). Although the distributions of capacitance (single Gaussian R^2 = 0.8756, two Gaussian fit not estimable; Figure 3H), membrane resistance (single Gaussian R^2 = 0.5422, two Gaussian fit not estimable; Figure 3I), and AP threshold (single Gaussian R^2 = 0.7711, two Gaussian fit not estimable; Figure 3J) for PV+ neurons appeared skewed and/or bimodal, the presence of other PV+ subtypes based on these membrane properties was not revealed. The passive and active membrane properties we assessed for PV− type III neurons exhibited unimodal distributions: spike accommodation (single Gaussian R^2 = 0.9497, two Gaussian fit not estimable; Figure 3E), maximum firing rate (single Gaussian R^2 = 0.9758, two Gaussian fit not estimable; Figure 3F), resting membrane voltage (single Gaussian R^2 = 0.7585, two Gaussian fit not estimable; Figure 3G), capacitance (single Gaussian R^2 = 0.9157, two Gaussians R^2 = 0.9568, F[3, 5] = 1.587, P = 0.3036; Figure 3H), membrane resistance (single Gaussian R^2 = 0.9185, two Gaussian fit not estimable; Figure 3I), and AP threshold (single Gaussian R^2 = 0.9543, two Gaussian fit not estimable; Figure 3J). Thus, we did not detect any further subtypes of interneurons using these measures.

Comparison of membrane properties of five different claustrum neuron subtypes

To test the veracity of our neuron classification, we next compared the passive and active membrane properties for the five different claustrum neuron subtypes against each other. Type II neurons displayed significantly larger capacitance values relative to all other neuron subtypes, followed by type I neurons, which had significantly higher capacitance than the three aspiny subtypes. We also observed that PV+ type IV neurons exhibited lower capacitance than PV− type III neurons (ANOVA, F[4, 146] = 164.2, P < 0.0001; Figure 4A). With regard to resting membrane voltage, PV+ type V aspiny neurons were significantly more depolarized relative to all other neuron subtypes (ANOVA, F[4, 184] = 8.392, P < 0.0001; Figure 4B). PV+ type V and PV− type III aspiny neurons exhibited significantly higher membrane resistance compared to type I and II spiny neurons, as well as PV+ type IV aspiny neurons (ANOVA, F[4, 184] = 19.86, P < 0.0001; Figure 4C). The difference in membrane resistance between PV+ type IV and V neurons reflects the particularly wide distribution that PV+ neurons exhibited for this measure (Figure 3I).

Consistent with their fast-spiking profile, PV+ type IV aspiny neurons displayed significantly lower spike accommodation index (ANOVA, F[4, 112] = 10.56, P < 0.0001) and higher maximum firing rate (ANOVA, F[4, 112] = 116.8, P < 0.0001) relative to the other claustrum neuron subtypes (Figure 4D, 4E). Interestingly, a significantly higher proportion of PV+ type IV and V aspiny neurons exhibited spontaneous AP firing relative to the other three claustrum neuron subtypes (X^2[4] = 46.14, P < 0.001; Figure 4F). Type IV neurons also demonstrated a significantly hyperpolarized threshold for AP generation compared to all other neuron types (ANOVA, F[4, 125] = 2.563, P = 0.0416; Figure 4G). A scatter plot of electrophysiological measures that differentiate claustrum neuron types by capacitance, membrane resistance, and firing rate and the observed proportion of each neuron type are shown in Figure 4H-4I. Figure 4I includes neurons recorded using both potassium-based and cesium-based internal pipette solutions.

Burst firing of claustrum projection neurons in response to ACC afferent drive is type-specific and intrinsic membrane property-mediated

Previous work in our laboratory demonstrates that spiny claustrum projection neurons exhibit burst firing in response to ACC afferent stimulation (White et al. 2018). If this burst firing is a defining feature of all spiny claustrum neurons or specifically restricted to type I or II neurons is unclear. Moreover, how burst firing is generated is unexplored. In order to address the first issue, we stimulated ACC afferents expressing ChR2 (see Figure 1A-1B) with 470 nm light (Figure 5A) while recording from the two spiny projection neuron subtypes in normal artificial cerebral spinal fluid (aCSF). In response to ACC afferent stimulation, we observed burst firing in a smaller proportion of type I neurons compared to type II neurons (Fisher's exact test, $P = 0.0198$; Figure 5B-5C). As such, the ACC input signal amplified by claustrum, and ultimately destined for cortex, is mediated primarily by type II claustrum neurons.

In order to assess intrinsic burst firing from claustrum projection neurons, we delivered a brief depolarizing voltage step without any stimulation of ACC afferents and observed burst firing in most neurons ($n = 8$ of 13). These recordings included both type I and II neurons, and the proportion of neurons showing intrinsic burst firing did not differ from the total proportion of spiny neurons that burst fired in response to ACC afferent stimulation ($n = 12$ of 20; Fisher's exact test $p = 1.0$). In pyramidal neurons, fast membrane repolarization mediated by voltage-gated potassium channels optimizes burst firing frequency (Brumberg et al. 2000; Gu et al. 2007). To test a similar mechanism, we washed on TEA-Cl at a low concentration and examined the inter-spike interval of APs in burst-firing spiny neurons before and after TEA-Cl treatment (Figure 5D). TEA-Cl lengthened the inter-spike interval relative to baseline (paired t test, $t[11] = 3.809$, $P = 0.0029$; Figure 5E). To control for effects of time and/or induction of multiple bursts, we performed a control wash of normal aCSF in separate cells and found no effect on inter-spike interval compared to baseline (paired t test, $t[7] = 1.183$, $P = 0.2755$; Figure 5E).

In pyramidal neurons, burst firing requires Ca^{2+} conductance (Williams and Stuart 1999). In order to test this requirement, we identified burst-firing claustrum neurons and then washed on aCSF without Ca^{2+}. In the absence of Ca^{2+}, burst firing was abolished (Figure 5F; $n = 6$ of 6). To determine the identity of the voltage-gated calcium channels (VGCC), we delivered a voltage step (−60 to −10 mV) using an internal pipette solution with voltage-gated sodium and potassium channel blockers present to isolate VGCC current (Figure 5G). We recorded the resulting current magnitude in the presence of various VGCC blockers: NNC 55-0396 (T-type), Blocker VIII (L-type, 1.3 specific), Nifedipine (L-type), $NiCl_2$ (R- and T-type), ω-conotoxin GVIA (N-type), and ω-agatoxin IVA (P/Q-type). We found that the magnitude was less only in the presence of ω-conotoxin GVIA (unpaired t test, $t[50] = 3.589$, $P = 0.0008$) and ω-agatoxin IVA (unpaired t test, $t[50] = 2.616$, $P = 0.0117$) compared to normal aCSF (Figure 5H). These results indicate that N- and P/Q-type calcium channels comprise a significant proportion of the observed VGCC current. In the absence of Ca^{2+} we detected negligible current (unpaired t test, $t[50] = 6.503$, $P < 0.0001$), confirming that our measurements were in fact VGCC currents (Figure 5H). If differences in Ca^{2+} flux explain the preferential burst firing of type II neurons in response to ACC afferent stimulation, then

VGCC current magnitude should dissociate type I and II neurons. We examined VGCC current magnitude in both types I and II neurons (Figure 5I, n =44) and found that capacitance, which defines types I and II, was strongly correlated with VGCC current magnitude (R^2 = 0.5836, P < 0001; Figure 5J). Additionally, we found that VGCC current magnitude exhibited a bimodal distribution (single Gaussian R^2 = 0.6040, two Gaussians R^2 = 0.9444, F[3, 7] = 14.29, P = 0.0023; Figure 5K) similar to that observed for capacitance (see Figure 2A). Parameters from the two Gaussian fit established distributions around 645 ± 186 pA (mean ± SD) and 1214 ± 109 pA (mean ± SD).

Claustrum projection neurons differentially target cortex

Claustrum connections with cortex are notably widespread (Crick and Koch 2005; Mathur 2014). As such, we next sought to interrogate whether the two types of claustrum projection neurons, which show differential processing of ACC input, show differential targeting of cortex. To test this, we injected retrogradely-transported biotinylated dextran amine (retro-BDA; 3,000 MW) into different cortical areas along the cortical hierarchy in different animals, including primary/secondary visual cortices (V1/V2), parietal association cortex (PtA), and ACC (Figure 6A). Retrogradely-labeled neurons in claustrum were targeted for whole-cell patch clamp electrophysiology (Figure 6B) and categorized as type I or II neurons based on their capacitance (see Figure 2A). We found that 75% of claustrum neurons projecting to V1/V2 were type I neurons, whereas 25% were type II neurons (n = 12; Figure 6C). Of the claustrum neurons projecting to PtA, 43% were type I and 57% were type II (n = 14; Figure 6D). Finally, of the claustrum neurons projecting to ACC, only 21% were type I and 79% were type II (n = 14; Figure 6E). The breakdown of type I and II neurons was different between V1/V2 and ACC (Fisher's exact test, P = 0.016) but not different between V1/V2 and PtA (Fisher's exact test, P = 0.13) or between PtA and ACC (Fisher's Exact test, P = 0.42).

Discussion

These data support the existence of five neuron types in the claustrum based on functional membrane properties. Type I neurons are spiny projection neurons with relatively low capacitance and smaller VGCC current amplitude that seldom burst fire in response to ACC afferent stimulation. In contrast, type II projection neurons possess higher capacitance and larger VGCC current amplitude relative to their type I counterparts. In addition, type II neurons exhibit more spike accommodation at the onset of a depolarizing current injection relative to type I neurons, and type II neurons burst fire readily in response to ACC afferent stimulation. We find that voltage-gated potassium channels enhance the burst firing frequency and that burst firing requires Ca^{2+} which is similar to burst firing mechanisms in cortical neurons (Williams and Stuart 1999; Brumberg et al. 2000). Moreover, most claustrum neurons projecting to V1/V2 are type I, about equal numbers of type I and II project to PtA, and most neurons projecting to ACC are type II. We also delineate three interneuron subtypes. In particular, type III neurons do not express PV and are not tonically active at rest, nor are these neurons fast-spiking. Both type IV and V neurons express PV and are tonically active, but type IV neurons are not capable of firing at the same maximum firing rates as their type V counterparts.

Our approach to visualize the dense ACC terminal field in claustrum to localize the structure provides a means to unambiguously distinguish claustrum from surrounding insular cortex (White et al. 2017). Further confirming that our electrophysiological recordings were not performed in the insular cortex, our claustrum neuron functional property data differ in many ways from that of cortical neurons. For instance, spiny claustrum neurons have a more depolarized resting membrane potential and AP threshold, as well as a higher membrane resistance compared to cortical pyramidal neurons (Yang et al. 1996). Additionally, spiny claustrum neurons exhibit radially-extending dendrites without a notable apical dendrite as in pyramidal neurons, consistent with extant data (Watakabe et al. 2014).

Our finding that an executive area of cortex, such as ACC, receives more type II claustrum neuron input, whereas a primary/secondary area of cortex, such as V1/V2, receives more type I input may inform our understanding of claustrum function. For instance, ACC excitation of claustrum may elicit a particularly strong excitatory feedback response due to the propensity of type II claustrum neurons to burst fire (Kim and McCormick 1998; Williams and Stuart 1999). Effects of claustrum on V1/V2 activity may be comparatively weaker, and effects on PtA may be intermediate to those on V1/V2 and ACC. An important consideration for interpreting our results is that type I and II neurons may not be evenly distributed across claustrum. For instance, caudal claustrum may be composed of more type I neurons and preferentially connect with V1/V2. However, this is unlikely because claustrum projections to cortex in rodent show an even distribution across the claustrum's rostrocaudal axis (White et al., 2017). More plausibly, type I and II neurons may target different layers of cortex, as claustrum does not innervate all cortices in that same fashion (Wang et al. 2017). For example, type I neurons may specifically target layer VI and claustrum may preferentially target layer VI of V1/V2. However, any innervation differences between type I and II claustrum neurons at present is entirely speculative, and more work is needed to resolve these innervation differences. Future work is also necessary to identify strategies to specifically manipulate type I or II neurons *in* vivo. Identifying unique protein expression profiles of subclasses of projection neurons, which have been found in cortical neurons based on projection targets (Arlotta et al. 2005; Sugino et al. 2006; Watakabe et al. 2012; Sorensen et al. 2015), is a critical first step in this regard.

Our data support the existence of three aspiny interneuron subtypes (types III-V) in the adult mouse claustrum, which supports and extends a previous report in brain slices taken from juvenile mice (Kim et al. 2016). Gathering genome-wide RNA sequencing of individual claustrum neurons and associating these data with neurophysiological data will eventually reveal the full panoply of cell diversity in the claustrum (Macosko et al. 2015). Such analysis would at least divide type III neurons into subclasses based perhaps on calcium binding protein markers, signaling neuropeptides, and enzymes including PV, calbindin, calretinin, somatostatin, vasoactive intestinal peptide, neuropeptide Y, cholecystokinin, and nitric oxide synthase (Eiden et al. 1990; Kowiański et al. 2001, 2003, 2008; Pirone et al. 2014).

Using basic neurophysiological features that are widely applied in neuroscience to define adult claustrum neuronal subtypes provides a critical springboard to launch more detailed investigations. For instance, although morphological distinctions between spiny neurons have not been reported (Brand 1981; LeVay and Sherk 1981; Dinopoulos et al. 1992;

Watakabe et al. 2014), a more fine-grained analysis such as quantification of spine volume/density may reveal differences between type I and type II neurons consistent with the differences in capacitance we observe. Similarly, future studies may uncover if the small population of interneurons with sparse dendritic branching (Brand 1981; LeVay and Sherk 1981; Dinopoulos et al. 1992) correspond to an interneuron subtype defined by electrophysiological properties, such as PV+ type IV neurons. In addition, electrophysiological analyses of synaptic plasticity mechanisms or changes in intrinsic membrane properties of spiny projection neurons in response to experience or drug challenge are now possible. Constructing claustrum microcircuitry incorporating all five neuron types will be critical to fully understanding the nature of claustrum processing of cortical input. Given the massive projection into the claustrum from the ACC and possibly other cingulate cortices (Smith and Alloway 2010; White et al. 2017), plastic changes at these synapses onto claustrum neurons may critically shape claustrum responsivity to ACC input. These plastic changes would reflect similar phenomena that occur at the corticostriatal synapse in the neighboring dorsal striatum (Mathur et al. 2011; Ellender et al. 2011; Mathur and Lovinger 2012; Atwood et al. 2014). Ultimately, probing plasticity of ACC inputs to claustrum may enhance our understanding of top-down cognitive control in health and disease states involving frontal executive dysfunction, such as schizophrenia, mood disorders and addiction (Levin 1984; Callicott et al. 2000; Marvel and Paradiso 2004; Cho et al. 2006; Minzenberg et al. 2009; Crews and Boettiger 2009; Goldstein and Volkow 2011).

Acknowledgments:

This work has been supported by National Institute on Alcohol Abuse and Alcoholism grants K22AA021414 and R01AA024845 (B.N.M.), a Whitehall Foundation grant 2014-12-68 (B.N.M.), National Institute of General Medical Sciences grant T32GM008181 (M.G.W.), National Institute of Neurological Disorders and Stroke grant T32NS063391 (M.G.W.), and National Institute of Mental Health grant F31MH112350 (M.G.W.).

References

Arlotta P, Molyneaux BJ, Chen J, et al. (2005) Neuronal Subtype-Specific Genes that Control Corticospinal Motor Neuron Development In Vivo. Neuron 45:207–221. doi: 10.1016/j.neuron.2004.12.036 [PubMed: 15664173]

Atlan G, Terem A, Peretz-Rivlin N, et al. (2017) Mapping synaptic cortico-claustral connectivity in the mouse. J Comp Neurol 525:1381–1402. doi: 10.1002/cne.23997 [PubMed: 26973027]

Atwood BK, Kupferschmidt DA, Lovinger DM (2014) Opioids induce dissociable forms of long-term depression of excitatory inputs to the dorsal striatum. Nat Neurosci 17:540–8. doi: 10.1038/nn.3652 [PubMed: 24561996]

Bernstein H-G, Ortmann A, Dobrowolny H, et al. (2016) Bilaterally reduced claustral volumes in schizophrenia and major depressive disorder: a morphometric postmortem study. Eur Arch Psychiatry Clin Neurosci 266:25–33. doi: 10.1007/S00406-015-0597-x [PubMed: 25822416]

Braak H, Braak E (1982) Neuronal types in the claustrum of man. Anat Embryol (Berl) 163:447–60 [PubMed: 7091711]

Brand S (1981) A serial section Golgi analysis of the primate claustrum. Anat Embryol 162:475–88 [PubMed: 6181715]

Brumberg JC, Nowak LG, McCormick DA (2000) Ionic mechanisms underlying repetitive high-frequency burst firing in supragranular cortical neurons. J Neurosci 20:4829–43 [PubMed: 10864940]

Callicott JH, Bertolino A, Mattay VS, et al. (2000) Physiological Dysfunction of the Dorsolateral Prefrontal Cortex in Schizophrenia Revisited. Cereb Cortex 10:1078–1092. doi: 10.1093/cercor/10.11.1078 [PubMed: 11053229]

Cho RY, Konecky RO, Carter CS (2006) Impairments in frontal cortical synchrony and cognitive control in schizophrenia. Proc Natl Acad Sci 103:19878–19883. doi: 10.1073/pnas.0609440103 [PubMed: 17170134]

Cozzi B, Roncon G, Granato A, et al. (2014) The claustrum of the bottlenose dolphin Tursiops truncatus (Montagu 1821). Front Syst Neurosci 8:42. doi: 10.3389/fnsys.2014.00042 [PubMed: 24734007]

Crews FT, Boettiger CA (2009) Impulsivity, frontal lobes and risk for addiction. Pharmacol Biochem Behav 93:237–247. doi: 10.1016/j.pbb.2009.04.018 [PubMed: 19410598]

Crick FC, Koch C (2005) What is the function of the claustrum? Philos Trans R Soc B Biol Sci 360:1271–1279. doi: 10.1098/rstb.2005.1661

Dávila JC, Real MÁ, Olmos L, et al. (2005) Embryonic and postnatal development of GABA, calbindin, calretinin, and parvalbumin in the mouse claustral complex. J Comp Neurol 481:42–57. doi: 10.1002/cne.20347 [PubMed: 15558732]

Dinopoulos A, Papadopoulos GC, Michaloudi H, et al. (1992) Claustrum in the hedgehog (Erinaceus europaeus) brain: Cytoarchitecture and connections with cortical and subcortical structures. J Comp Neurol 316:187–205. doi: 10.1002/cne.903160205 [PubMed: 1374084]

Druckmann S, Banitt Y, Gidon A, et al. (2007) A novel multiple objective optimization framework for constraining conductance-based neuron models by experimental data. Front Neurosci 1:7–18. doi: 10.3389/neuro.01.1.1.001.2007 [PubMed: 18982116]

Eiden LE, Mezey E, Eskay RL, et al. (1990) Neuropeptide content and connectivity of the rat claustrum. Brain Res 523:245–50 [PubMed: 1976024]

Ellender TJ, Huerta-Ocampo I, Deisseroth K, et al. (2011) Differential Modulation of Excitatory and Inhibitory Striatal Synaptic Transmission by Histamine. J Neurosci 31:15340–15351. doi: 10.1523/JNEUROSCI.3144-11.2011 [PubMed: 22031880]

Goldstein RZ, Volkow ND (2011) Dysfunction of the prefrontal cortex in addiction: neuroimaging findings and clinical implications. Nat Rev Neurosci 12:652–669. doi: 10.1038/nrn3119 [PubMed: 22011681]

Gu N, Vervaeke K, Storm JF (2007) BK potassium channels facilitate high-frequency firing and cause early spike frequency adaptation in rat CA1 hippocampal pyramidal cells. J Physiol 580:859–882. doi: 10.1113/jphysiol.2006.126367 [PubMed: 17303637]

Hinova-Palova DV, Edelstein L, Landzhov BV., et al. (2014) Parvalbumin-immunoreactive neurons in the human claustrum. Brain Struct Funct 219:1813–1830. doi: 10.1007/s00429-013-0603-x [PubMed: 23832597]

Hur EE, Zaborszky L (2005) Vglut2 afferents to the medial prefrontal and primary somatosensory cortices: a combined retrograde tracing in situ hybridization study [corrected], J Comp Neurol 483:351–73. doi: 10.1002/cne.20444 [PubMed: 15682395]

Kim J, Matney CJ, Roth RH, Brown SP (2016) Synaptic Organization of the Neuronal Circuits of the Claustrum. J Neurosci 36:773–84. doi: 10.1523/JNEUROSCI.3643-15.2016 [PubMed: 26791208]

Kim U, McCormick DA (1998) The functional influence of burst and tonic firing mode on synaptic interactions in the thalamus. J Neurosci 18:9500–16 [PubMed: 9801387]

Kong L, Bachmann S, Thomann PA, et al. (2012) Neurological soft signs and gray matter changes: A longitudinal analysis in first-episode schizophrenia. Schizophr Res 134:27–32. doi: 10.1016/j.schres.2011.09.015 [PubMed: 22018942]

Kowiański P, Dziewiatkowski J, Moryś JM, et al. (2009) Colocalization of neuropeptides with calcium-binding proteins in the claustral interneurons during postnatal development of the rat. Brain Res Bull 80:100–6. doi: 10.1016/j.brainresbull.2009.06.020 [PubMed: 19576270]

Kowiański P, Moryś JM, Dziewiatkowski J, et al. (2008) NPY-, SOM- and VIP-containing interneurons in postnatal development of the rat claustrum. Brain Res Bull 76:565–71. doi: 10.1016/j.brainresbull.2008.04.004 [PubMed: 18598846]

Kowiański P, Moryś JM, Wójcik S, et al. (2003) Co-localisation of NOS with calcium-binding proteins during the postnatal development of the rat claustrum. Folia Morphol (Warsz) 62:211–4 [PubMed: 14507049]

Kowiański P, Timmermans JP, Moryś J (2001) Differentiation in the immunocytochemical features of intrinsic and cortically projecting neurons in the rat claustrum -- combined immunocytochemical and axonal transport study. Brain Res 905:63–71 [PubMed: 11423080]

Kupferschmidt DA, Cody PA, Lovinger DM, Davis MI (2015) Brain BLAQ: Post-hoc thick-section histochemistry for localizing optogenetic constructs in neurons and their distal terminals. Front Neuroanat 9:6. doi: 10.3389/fnana.2015.00006 [PubMed: 25698938]

LeVay S, Sherk H (1981) The visual claustrum of the cat. I. Structure and connections. J Neurosci 1:956–80 [PubMed: 6169810]

Levin S (1984) Frontal lobe dysfunctions in schizophrenia—II. impairments of psychological and brain functions. J Psychiatr Res 18:57–72. doi: 10.1016/0022-3956(84)90047-5 [PubMed: 6371224]

Macosko EZ, Basu A, Satija R, et al. (2015) Highly Parallel Genome-wide Expression Profiling of Individual Cells Using Nanoliter Droplets. Cell 161:1202–1214. doi: 10.1016/j.cell.2015.05.002 [PubMed: 26000488]

Madisen L, Zwingman TA, Sunkin SM, et al. (2010) A robust and high-throughput Cre reporting and characterization system for the whole mouse brain. Nat Neurosci 13:133–140. doi: 10.1038/nn.2467 [PubMed: 20023653]

Marvel CL, Paradiso S (2004) Cognitive and neurological impairment in mood disorders. Psychiatr Clin North Am 27:19–36. doi: 10.1016/S0193-953X(03)00106-0 [PubMed: 15062628]

Mathur BN (2014) The claustrum in review. Front Syst Neurosci 8:48. doi: 10.3389/fnsys.2014.00048 [PubMed: 24772070]

Mathur BN, Capik NA, Alvarez VA, Lovinger DM (2011) Serotonin Induces Long-Term Depression at Corticostriatal Synapses. J Neurosci 31:7402–7411. doi: 10.1523/JNEUROSCI.6250-10.2011 [PubMed: 21593324]

Mathur BN, Caprioli RM, Deutch AY (2009) Proteomic analysis illuminates a novel structural definition of the claustrum and insula. Cereb Cortex 19:2372–9. doi: 10.1093/cercor/bhn253 [PubMed: 19168664]

Mathur BN, Lovinger DM (2012) Endocannabinoid-Dopamine Interactions in Striatal Synaptic Plasticity. Front Pharmacol 3:66. doi: 10.3389/fphar.2012.00066 [PubMed: 22529814]

Mathur BN, Tanahira C, Tamamaki N, Lovinger DM (2013) Voltage drives diverse endocannabinoid signals to mediate striatal microcircuit-specific plasticity. Nat Neurosci 16:1275–1283. doi: 10.1038/nn.3478 [PubMed: 23892554]

Minzenberg MJ, Laird AR, Thelen S, et al. (2009) Meta-analysis of 41 Functional Neuroimaging Studies of Executive Function in Schizophrenia. Arch Gen Psychiatry 66:811. doi: 10.1001/archgenpsychiatry.2009.91 [PubMed: 19652121]

Morys J, Bobinski M, Wegiel J, et al. (1996) Alzheimer's disease severely affects areas of the claustrum connected with the entorhinal cortex. J Hirnforsch 37:173–80 [PubMed: 8776503]

Patru MC, Reser DH (2015) A New Perspective on Delusional States - Evidence for Claustrum Involvement. Front psychiatry 6:158. doi: 10.3389/fpsyt.2015.00158 [PubMed: 26617532]

Pirone A, Castagna M, Granato A, et al. (2014) Expression of calcium-binding proteins and selected neuropeptides in the human, chimpanzee, and crab-eating macaque claustrum. Front Syst Neurosci 8:99. doi: 10.3389/fnsys.2014.00099 [PubMed: 24904320]

Pirone A, Magliaro C, Giannessi E, Ahluwalia A (2015) Parvalbumin expression in the claustrum of the adult dog. An immunohistochemical and topographical study with comparative notes on the structure of the nucleus. J Chem Neuroanat 64–65:33–42. doi: 10.1016/j.jchemneu.2015.02.004

Rahman FE, Baizer JS (2007) Neurochemically defined cell types in the claustrum of the cat. Brain Res 1159:94–111. doi: 10.1016/j.brainres.2007.05.011 [PubMed: 17582386]

Real MA, Dávila JC, Guirado S (2003) Expression of calcium-binding proteins in the mouse claustrum. J Chem Neuroanat 25:151–60 [PubMed: 12706203]

Reynhout K, Baizer JS (1999) Immunoreactivity for calcium-binding proteins in the claustrum of the monkey. Anat Embryol (Berl) 199:75–83 [PubMed: 9924937]

Smith JB, Alloway KD (2010) Functional Specificity of Claustrum Connections in the Rat: Interhemispheric Communication between Specific Parts of Motor Cortex. J Neurosci 30:16832–16844. doi: 10.1523/JNEUROSCI.4438-10.2010 [PubMed: 21159954]

Sorensen SA, Bernard A, Menon V, et al. (2015) Correlated Gene Expression and Target Specificity Demonstrate Excitatory Projection Neuron Diversity. Cereb Cortex 25:433–449. doi: 10.1093/cercor/bht243 [PubMed: 24014670]

Sugino K, Hempel CM, Miller MN, et al. (2006) Molecular taxonomy of major neuronal classes in the adult mouse forebrain. Nat Neurosci 9:99–107. doi: 10.1038/nn1618 [PubMed: 16369481]

Szalak R, Matysek M, Mozel S, Arciszewski MB (2015) Immunocytochemical detection of calretinin in the claustrum and endopiriform nucleus of the chinchilla. Pol J Vet Sci 18:857–63. doi: 10.1515/pjvs-2015-0111 [PubMed: 26812830]

Tanahira C, Higo S, Watanabe K, et al. (2009) Parvalbumin neurons in the forebrain as revealed by parvalbumin-Cre transgenic mice. Neurosci Res 63:213–223. doi: 10.1016/j.neures.2008.12.007 [PubMed: 19167436]

Wang Q, Ng L, Harris JA, et al. (2017) Organization of the connections between claustrum and cortex in the mouse. J Comp Neurol 525:1317–1346. doi: 10.1002/cne.24047 [PubMed: 27223051]

Watakabe A, Hirokawa J, Ichinohe N, et al. (2012) Area-specific substratification of deep layer neurons in the rat cortex. J Comp Neurol 520:3553–3573. doi: 10.1002/cne.23160 [PubMed: 22678985]

Watakabe A, Ohsawa S, Ichinohe N, et al. (2014) Characterization of claustral neurons by comparative gene expression profiling and dye-injection analyses. Front Syst Neurosci 8:98. doi: 10.3389/fnsys.2014.00098 [PubMed: 24904319]

White MG, Cody PA, Bubser M, et al. (2017) Cortical hierarchy governs rat claustrocortical circuit organization. J Comp Neurol 525:1347–1362. doi: 10.1002/cne.23970 [PubMed: 26801010]

White MG, Mathur BN (2018) Frontal cortical control of posterior sensory and association cortices through the claustrum. Brain Struct Funct 1–8. doi: 10.1007/S00429-018-1661-x [PubMed: 29222724]

White MG, Panicker M, Mu C, et al. (2018) Anterior Cingulate Cortex Input to the Claustrum Is Required for Top-Down Action Control. Cell Rep 22:84–95. doi: 10.1016/j.celrep.2017.12.023 [PubMed: 29298436]

Williams SR, Stuart GJ (1999) Mechanisms and consequences of action potential burst firing in rat neocortical pyramidal neurons. J Physiol 521 Pt 2:467–82. doi: 10.1111/J.1469-7793.1999.00467.X [PubMed: 10581316]

Wójcik S, Dziewiatkowski J, Spodnik E, et al. (2004) Analysis of calcium binding protein immunoreactivity in the claustrum and the endopiriform nucleus of the rabbit. Acta Neurobiol Exp (Wars) 64:449–60 [PubMed: 15586661]

Yang CR, Seamans JK, Gorelova N (1996) Electrophysiological and morphological properties of layers V-VI principal pyramidal cells in rat prefrontal cortex in vitro. J Neurosci 16:1904–21 [PubMed: 8774458]

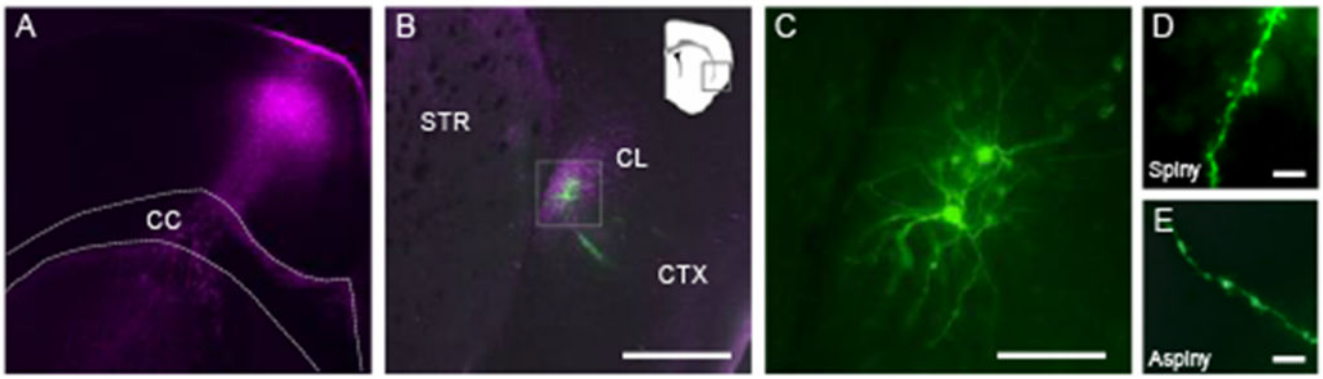

Figure 1. Identification of claustrum using fluorescently-labeled anterior cingulate cortex (ACC) afferents.

(A) Photomicrograph showing injection of adeno-associated virus expressing channelrhodopsin-2 and mCherry tag (purple, pseudo-colored) in ACC. The dotted lines outline the corpus callosum (CC). (B) Photomicrograph showing ACC afferents expressing mCherry (purple) in the contralateral claustrum (CL) and neurobiotin-filled spiny claustrum neurons (green) targeted for whole-cell electrophysiology. The neighboring cortex (CTX) and striatum (STR) are indicated and devoid of labeled fibers. (C) Inset from (B) showing the filled spiny claustrum neurons at higher magnification. (D-E) Photomicrograph showing a dendritic process from a spiny (D) or aspiny (E) claustrum neuron. Scale bars = 400 μm (B), 100 μm (C), 10 μm (D, E).

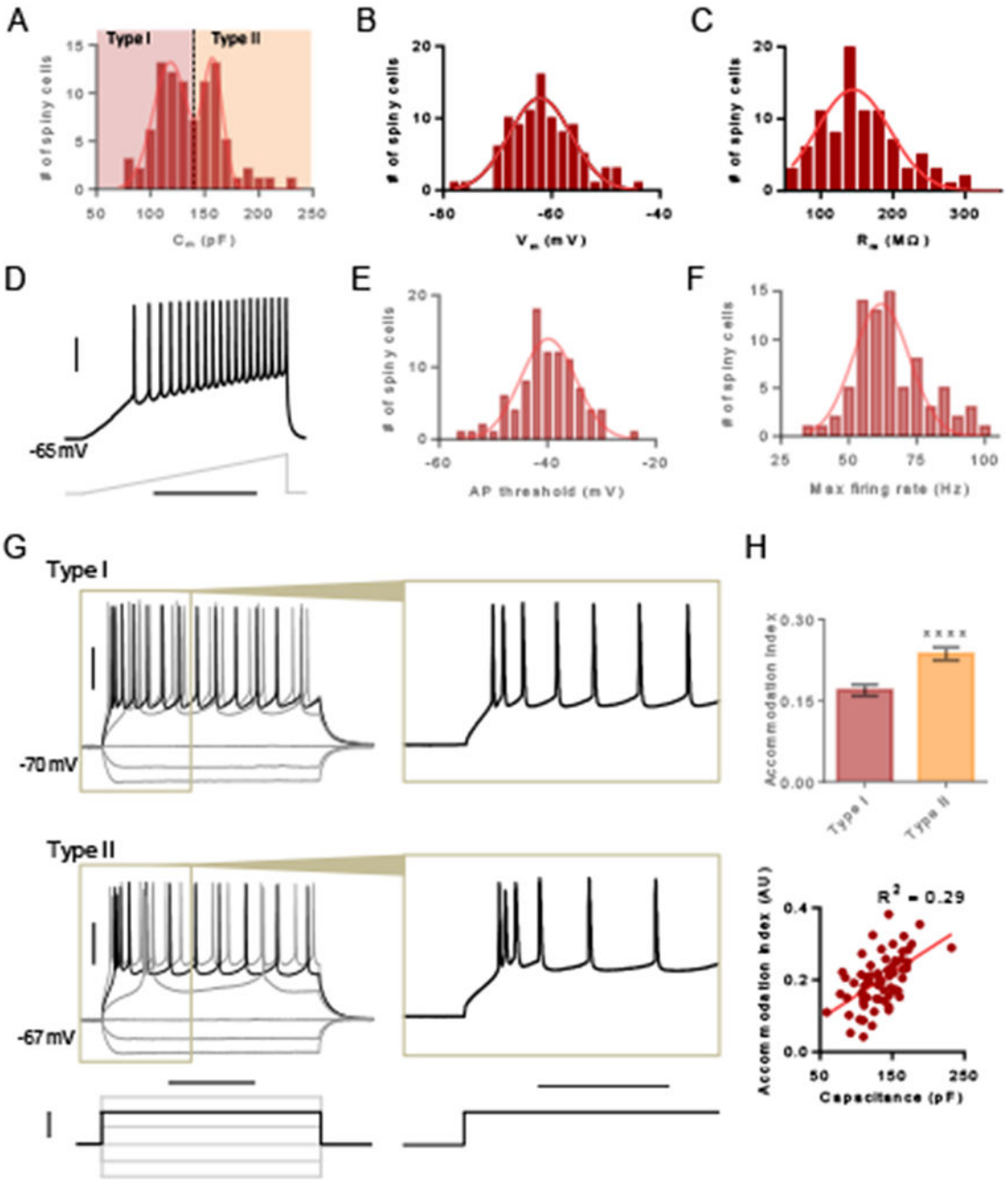

Figure 2. Membrane properties of spiny claustrum neurons delineate two subtypes.

(A) Histogram showing distribution of capacitance for spiny claustrum neurons. Type I neurons were defined as lower capacitance neurons and type II neurons were defined as higher capacitance neurons. (B) Histogram showing the distribution of resting membrane voltage. (C) Histogram showing the distribution of membrane resistance. (D) Representative trace showing a spiny claustrum neuron firing in response to a current injection ramp. (E) Histogram showing the distribution of the action potential (AP) threshold. (F) Histogram showing the distribution of the maximum firing rate. (G) Representative traces showing type

I (top) and type II (bottom) responses to various 500 ms current injection steps. Inset of black trace shows pattern of spike accommodation for APs occurring early in the step. (H) Accommodation index (AI) for the first 6 APs was larger for type II neurons compared to type I neurons (top) and AI correlated with capacitance (bottom). Unpaired *t* test, **** $P < 0.0001$. Horizontal scale bars = 400 ms (D), 200 ms (G [left]), 100 ms (G [right]). Vertical scale bars = 30 mV (D, G [top]), 200 pA (G [bottom]).

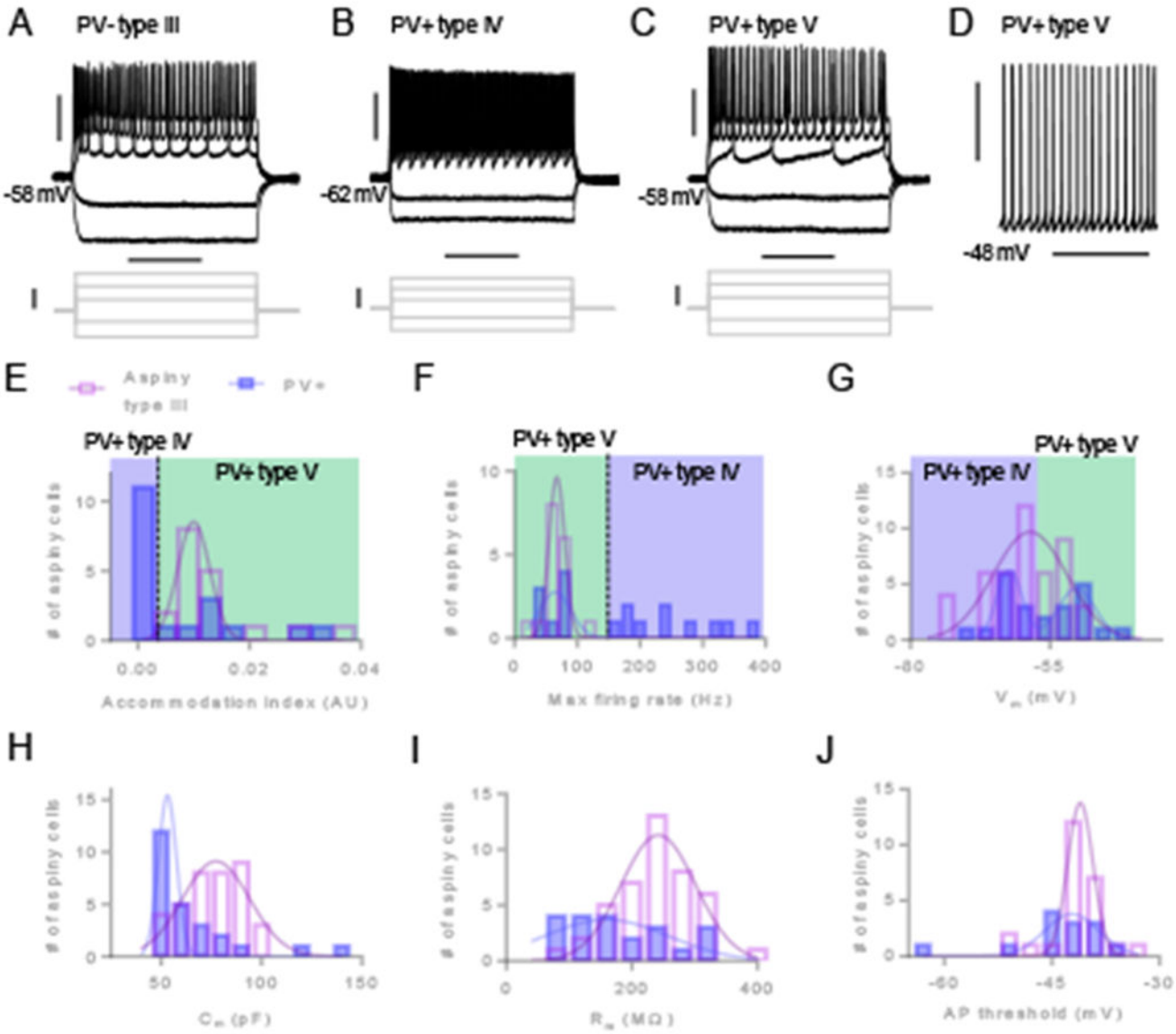

Figure 3. Membrane properties delineate three aspiny claustrum neuron types.

(A) Representative traces from a PV-negative (PV−) type III neuron showing responses to a series of 500 ms current injection steps. (B) Representative traces from a PV-positive (PV+) neuron showing fast-spiking in response to positive current injections, denoted as a type IV neuron. (C) Representative traces from a PV+ neuron that did not exhibit fast-spiking in response to positive current injections, denoted as a type V neuron. (D) Representative trace of a PV+ type V neuron that exhibited spontaneous firing of AP in the absence of current injection. (E) Histograms showing distributions of AI values for aspiny type III neurons (open purple bars) and PV+ neurons (filled blue bars). AI values for PV+ type IV and PV+ type V neurons are indicated by shaded blue area and green areas, respectively. (F) Histograms showing distributions of maximum firing rates for type III and PV+ neurons. (G) Histograms showing distributions of resting membrane voltage for type III and PV+

neurons. (H) Histograms showing distributions of capacitance for type III and PV+ neurons. (I) Histograms showing distributions of membrane resistance for type III and PV+ neurons. (J) Histograms showing distributions of AP threshold for type III and PV+ neurons. Horizontal scale bars = 200 ms (A, B, C), 3 s (D). Vertical scale bars = 30 mV (A [top], B [top], C [top], D), 200 pA (A [bottom], B [bottom], C [bottom]).

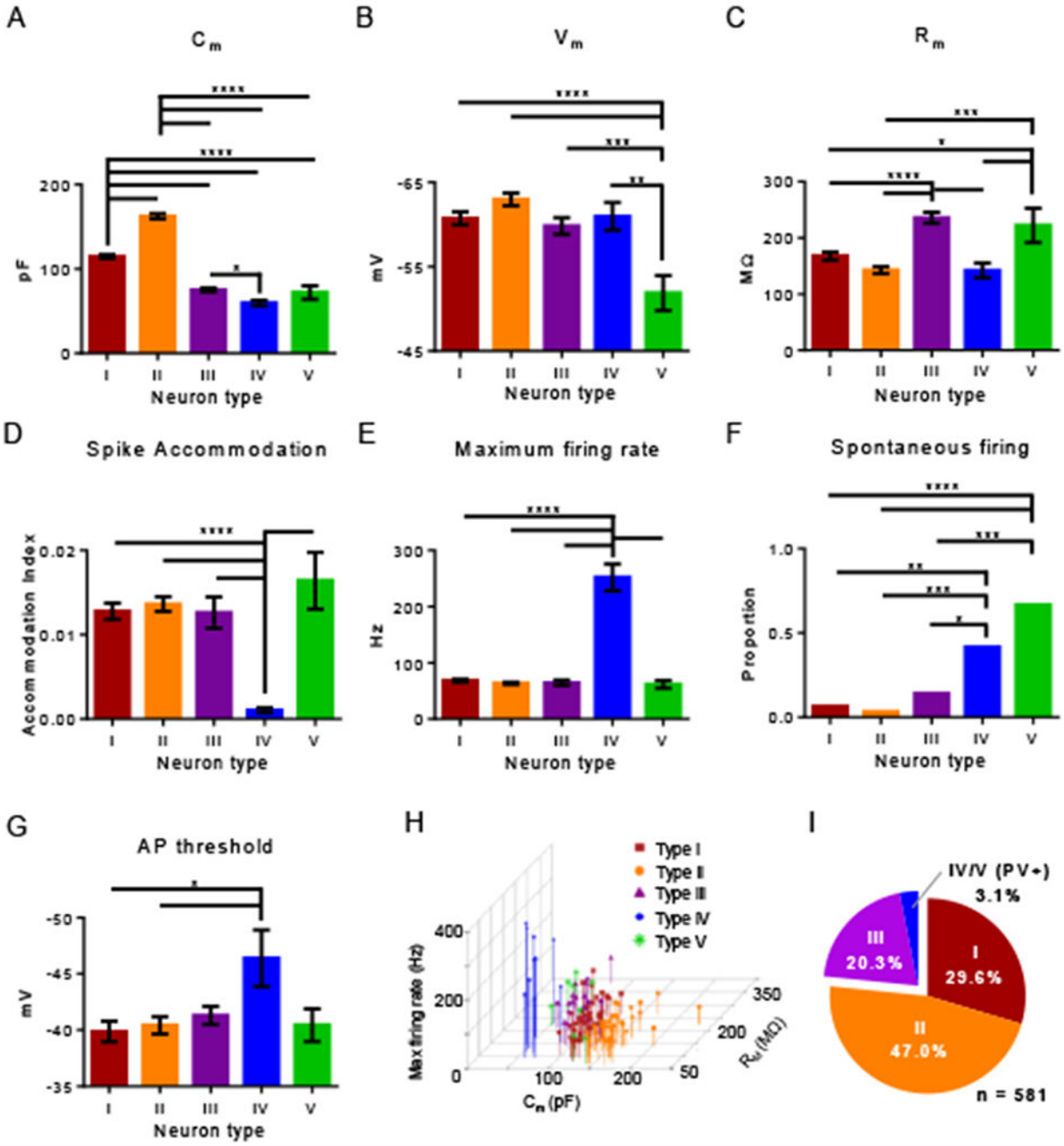

Figure 4. Comparison of membrane properties of claustrum neuron sub-types.

(A) Mean capacitance (C_m) varied significantly across claustrum neuron types (one-way ANOVA, $P < 0.0001$). Spiny type II neurons had greater mean capacitance relative to all other types, and spiny type I neurons had greater mean capacitance relative to the three aspiny types: III, IV and V. PV+ type IV neurons had a smaller capacitance relative to type III neurons. (B) Mean resting membrane potential (V_m) varied significantly across claustrum neuron types (one-way ANOVA, $P < 0.0001$). PV+ type V neurons were more depolarized relative to all other types. (C) Mean membrane resistance (R_m) varied significantly across

claustrum neuron types (one-way ANOVA, $P < 0.0001$). Aspiny PV− type III and PV+ type V neurons had greater mean membrane resistance compared to the other neuron types. (D) Mean spike accommodation index (AI), varied across neuron types (one-way ANOVA, $P < 0.0001$). AI of PV+ type IV neurons was less than all other neuron types. (E) Mean maximum firing rate varied across neuron types (one-way ANOVA, $P < 0.0001$). The firing rate of PV+ type IV neurons was greater than all other neuron types. (F) The proportion of PV+ type IV and V neurons that exhibited spontaneous firing was greater relative to the other claustrum neuron types. (G) Mean AP threshold varied across neuron type (one-way ANOVA, $P < 0.05$). Relative to spiny types I and II, the AP threshold for PV+ type IV neurons was significantly hyperpolarized. (H) Scatter plot of capacitance, resting membrane potential, and maximum firing rate of claustrum neuron types. These membrane properties most easily delineated the different claustrum neuron types. (I) Pie chart showing the relative percentages of each claustrum neuron type out of all claustrum neurons recorded. Post-hoc Tukey's test (A-E, G), * $P < 0.05$, ** $P < 0.01$, *** $P < 0.001$, **** $P < 0.0001$. Fisher's exact test (F), *** $P < 0.001$, **** $P < 0.0001$.

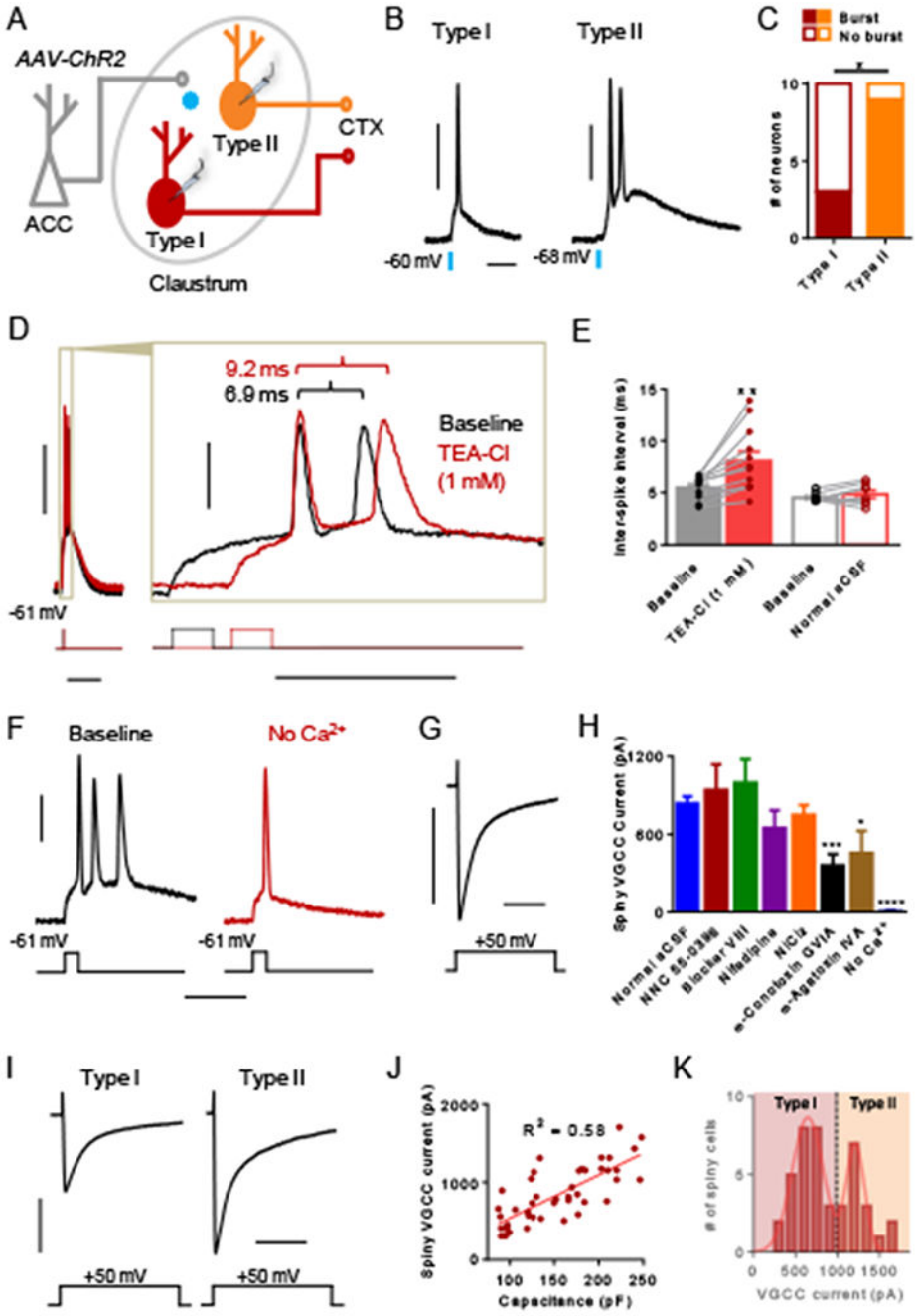

Figure 5. Spiny type II neurons preferentially burst fire in response to ACC input. Burst firing requires calcium and is optimized by voltage-gated potassium channels.

(A) Experimental schematic showing that ACC afferents in the claustrum expressing ChR2 were stimulated optogenetically with 470 nm light while recording responses from claustrum spiny type I and II neurons. (B) Representative traces showing single AP detonation from a type I neuron and an AP burst from a type II neuron in response to ACC afferent stimulation. (C) The proportion of type II neurons that burst fired in response to ACC afferent stimulation was greater than that of type I neurons. (D) Representative traces from a spiny claustrum neuron that burst fires in response to a brief depolarizing current

injection (5 ms) in normal aCSF (baseline, black trace) and after washing on TEA-Cl (1 mM, red trace). Inset illustrates that the inter-spike interval (ISI) became longer with TEA-Cl treatment. (E) TEA-Cl treatment (filled red bar) elicited a significantly longer ISI compared to baseline (filled black bar). Washing on normal aCSF (open red bar) did not change the ISI relative to baseline. (F) Representative trace from a spiny claustrum neuron showing that washing on aCSF without Ca^{2+} (red trace) abolishes burst firing present at baseline (black trace, $n = 6$ of 6). (G) Representative trace showing voltage-gated calcium channel (VGCC) current elicited in response to a voltage step (−60 to −10 mV). (H) The VGCC current magnitude in control conditions ($n = 44$) was compared to the magnitude in the presence of various VGCC blockers including NNC 55-0396 (15 μM, $n = 8$), blocker VIII (20 μM, $n = 8$), nifedipine (20 μM, $n = 11$), $NiCl_2$ (50 μM, $n = 17$), ω-conotoxin GVIA (1 μM, $n = 8$), ω-agatoxin IVA (200 nM, $n = 8$), and no Ca^{2+} ($n = 8$). (I) Representative traces of VGCC current measured from a type I and a type II spiny claustrum neuron. (J) Capacitance and VGCC current magnitude were significantly correlated for spiny claustrum neurons ($R^2 = 0.58$, $P < 0.0001$). (K) The distribution for VGCC magnitude was bimodal consistent with lower magnitude VGCC currents measured in type I neurons and higher magnitude currents measured in type II neurons. Fisher's exact test, * $P < 0.05$ (C); paired t test, ** $P < 0.01$ (E); unpaired t test, * $P < 0.05$, *** $P < 0.001$, **** $P < 0.0001$ (H). Horizontal scale bars = 20 ms (B), 100 ms (D [left]), 20 ms (D [right]), 20 ms (F), 200 ms (G, I). Vertical scale bars = 30 mV (B, D, F), 500 pA (G, I).

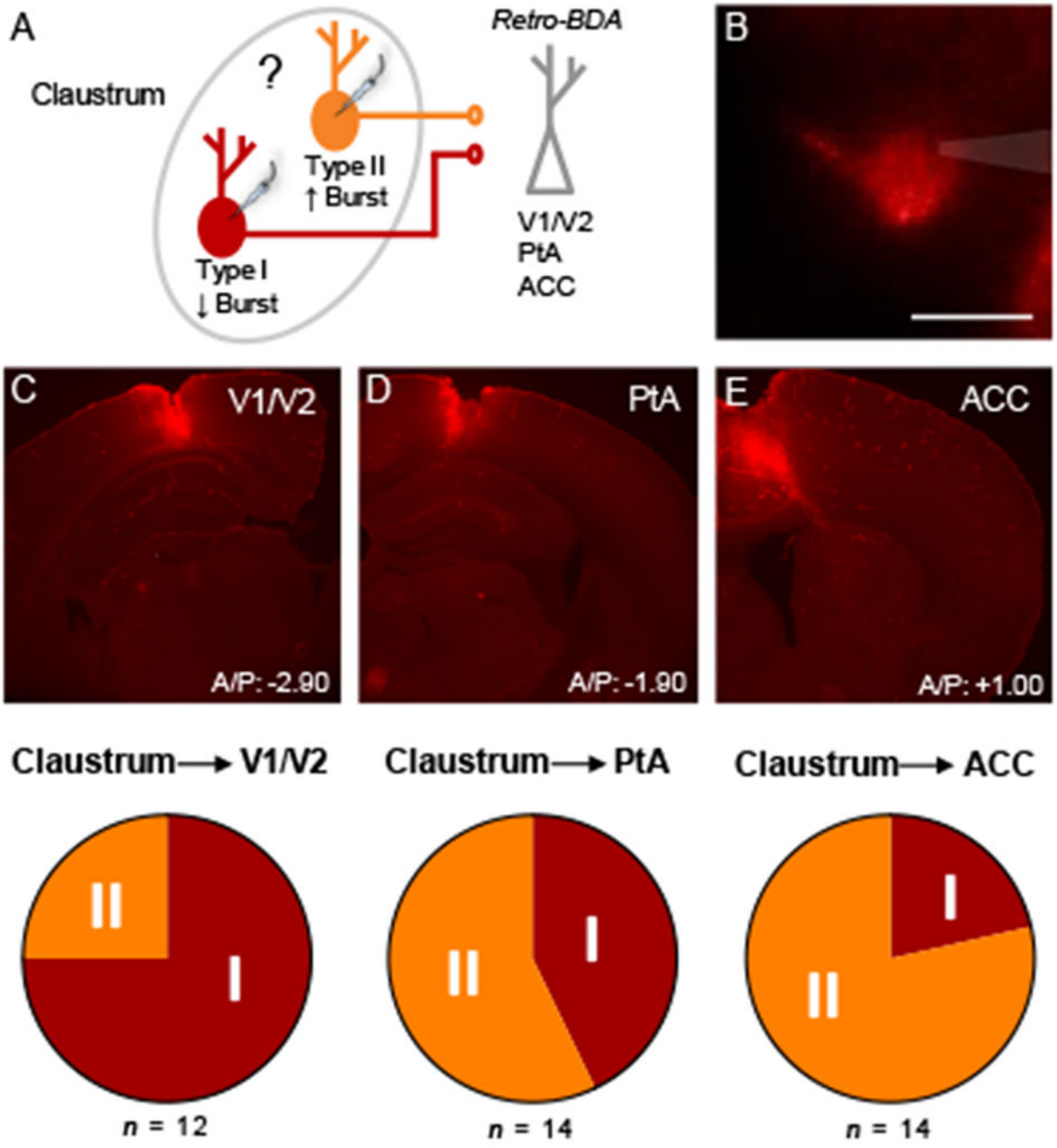

Figure 6. Type I and II claustrum neurons differentially target cortex.

(A) Experimental schematic showing that retrogradely-transported biotinylated dextran amine (retro-BDA; 3,000 MW) was injected into different cortices in different mice. Labeled claustrum neurons were classified as type I or II using whole-cell patch clamp electrophysiology. (B) Photomicrograph showing a retrogradely-labeled claustrum neuron (red) that was targeted for whole-cell patch clamp electrophysiology. The glass micropipette is shaded gray. (C) Top: Photomicrograph of retro-BDA injection into V1/V2. Bottom: 75% of claustrum neurons projecting to V1/V2 were type I and 25% were type II ($n = 12$). (D)

Top: Photomicrograph of retro-BDA injection into PtA. Bottom: 43% of claustrum neurons projecting to PtA were type I and 57% were type II ($n = 14$). (E) Top: Photomicrograph of retro-BDA injection into ACC. Bottom: 21% of claustrum neurons projecting to ACC were type I and 79% were type II ($n = 14$).